Emergent actin flows explain distinct modes of gliding motility

Check for updates

Christina L. Hueschen [1,8] ✉, Li-av Segev-Zarko [2], Jian-Hua Chen [3,4], Mark A. LeGros[3,4,5], Carolyn A. Larabell[3,4,5], John C. Boothroyd[2], Rob Phillips[6,7] & Alexander R. Dunn [1] ✉

During host infection, *Toxoplasma gondii* and related unicellular parasites move using gliding, which differs fundamentally from other known mechanisms of eukaryotic cell motility. Gliding is thought to be powered by a thin layer of flowing filamentous (F)-actin sandwiched between the plasma membrane and a myosin-covered inner membrane complex. How this surface actin layer drives the various gliding modes observed in experiments—helical, circular, twirling and patch, pendulum or rolling—is unclear. Here we suggest that F-actin flows arise through self-organization and develop a continuum model of emergent F-actin flow within the confines provided by *Toxoplasma* geometry. In the presence of F-actin turnover, our model predicts the emergence of a steady-state mode in which actin transport is largely directed rearward. Removing F-actin turnover leads to actin patches that recirculate up and down the cell, which we observe experimentally for drug-stabilized actin bundles in live *Toxoplasma gondii* parasites. These distinct self-organized actin states can account for observed gliding modes, illustrating how different forms of gliding motility can emerge as an intrinsic consequence of the self-organizing properties of F-actin flow in a confined geometry.

Single-celled parasites of the eukaryotic phylum Apicomplexa cause hundreds of millions of cases of malaria, toxoplasmosis and cryptosporidiosis each year[1–3]. To propel themselves over host cells and through extracellular matrix, motile Apicomplexa like *Plasmodium* spp. or *Toxoplasma gondii* use an adhesion-dependent locomotion mechanism called gliding that defies the paradigmatic classification of eukaryotic cells into cilia-dependent swimmers and cell-shape-change-dependent crawlers. Gliding depends on a layer of filamentous (F)-actin[4,5] and a fast, single-headed myosin, MyoA[6], confined to a 25-nm-thick compartment between the parasite plasma membrane and a membranous scaffold termed the inner membrane

complex (IMC)[7]. MyoA is anchored in the IMC through its association with myosin light chain 1 (MLC1)[7,8]. To drive gliding, MyoA is believed to slide short actin filaments rearward through the intermembrane space, towards the posterior end of the cell (reviewed in refs. 9,10). When actin-coupled adhesin proteins in the plasma membrane bind to a stationary external substrate, MyoA instead propels the inner cytoskeleton and parasite cytoplasm forward. The rearward direction of actin filament transport by MyoA was thought to be fixed and likely templated by a basket of polarized subpellicular microtubules beneath the IMC[9]. However, as discussed below, this 'templating' cannot account for all observed apicomplexan gliding motions.

¹Dept. of Chemical Engineering, Stanford University, Palo Alto, CA, USA. ²Dept. of Microbiology and Immunology, Stanford University, Palo Alto, CA, USA. ³Dept. of Anatomy, University of California San Francisco, San Francisco, CA, USA. ⁴National Center for X-ray Tomography, Lawrence Berkeley National Laboratory, Berkeley, CA, USA. ⁵Molecular Biophysics and Integrated Bioimaging Division, Lawrence Berkeley National Laboratory, Berkeley, CA, USA. ⁶Dept. of Physics, California Institute of Technology, Pasadena, CA, USA. ⁷Div. of Biology and Biological Engineering, California Institute of Technology, Pasadena, CA, USA. ⁸Present address: Dept. of Cell and Developmental Biology, University of California San Diego, La Jolla, CA, USA. ✉e-mail: chueschen@ucsd.edu; alex.dunn@stanford.edu
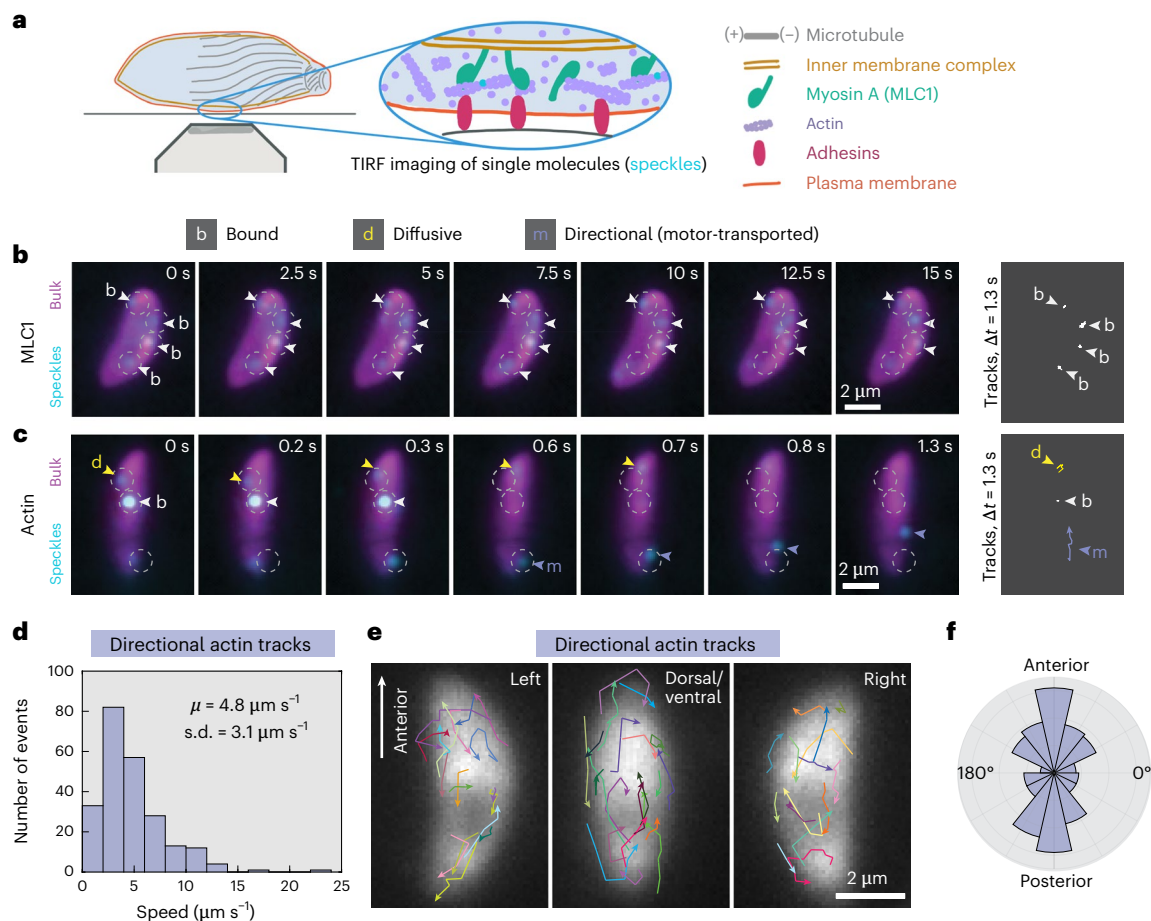
Fig. 1 | *Toxoplasma gondii* actin transport direction is heterogeneous, not uniformly rearward. a, Schematic of the intermembrane actomyosin layer that drives apicomplexan gliding and of TIRF imaging of speckle-labelled actin or MLC1. Inset: actin is speckle-labelled with single Janelia Fluor dyes (cyan). **b,c**, Examples of MLC1 (**b**) and actin (**c**) movement (speckles; cyan) over time in extracellular parasites, with higher-density labelling (bulk; magenta) to show cell position. Arrowheads highlight examples of specific protein behaviours. Images denoised with noise2void[60]. Protein trajectories (far right) are shown for an equal time interval (1.3 s) to allow comparison of bound (white), diffusive (yellow) and directional (purple) movements. Experiment repeated in *n* = 7 (MLC1) and *n* = 18

(actin) independent cells. **d**, Histogram of speeds of directional actin tracks from 18 cells. *μ*, mean; s.d., standard deviation. **e**, Directional actin tracks (*n* = 54 tracks in 18 overlaid cells from three experiments). Cells were grouped by the cell side visible, aligned with anterior end up and superimposed. Cell polarity was determined by microtubule labelling or tracking of the posterior end following posterior-down cell twirling (Supplementary Information Section 5), and directional actin tracks were aligned with respect to the parasite long axis. **f**, Polar histogram of the orientation of directional actin displacements with respect to cell polarity (*n* = 231 displacements, 54 tracks, 18 cells).

On a two-dimensional substrate, motile *Toxoplasma gondii* parasites can undergo helical gliding, with simultaneous forward translation and cell body rotation[11] (Supplementary Video 1), or glide in circles with their anterior (apical) end leading, motions that translate into a corkscrew trajectory when embedded in three-dimensional (3D) matrix[12–14]. These forward cell movements contributed to the working model of rearward actin transport along the path of subpellicular microtubules[9]. However, parasites also display a rotational motion known as twirling when oriented upright, with their posterior end on the substrate. In addition, observations of back-and-forth motion, termed patch or pendulum gliding, have been reported in a diversity of conditions (Supplementary Table 1, Supplementary Fig. 1a,b and Supplementary Video 1). Prevalent models of rearward-only actin transport cannot explain these motions. Further, MLC1 localizes throughout the IMC, not merely above subpellicular microtubules[15,16] (Supplementary Fig. 1c), making it unclear how myosin orientation might be fixed relative to the cell axis. Recent observations of unchanged gliding speeds in *Toxoplasma gondii* mutants with short and sparse microtubules[17], the discovery of gliding by *Plasmodium* merozoites[18], which do not have a basket of chiral subpellicular microtubules, and the observation of actin filament alignment to newly described IMC surface filaments in

Cryptosporidium parvum[19] further suggest that our understanding of how gliding motility arises from molecular-level organization remains incomplete. In this study, we sought to better understand how the actomyosin machinery gives rise to such a diverse array of gliding movements and, more broadly, how actin and myosin are patterned or polarized to yield coherent force generation in this system.

Tracking actin and myosin in motile *Toxoplasma gondii*

To directly test the model of 'templated' rearward actin transport along the path of subpellicular microtubules, we used fluorescent speckle imaging[20,21] to track actin (ACT1) and MLC1 proteins labelled with individual fluorophores in live, active *Toxoplasma gondii* tachyzoites (Fig. 1a). Pauses between parasite movements enabled us to reliably track protein movement (Methods) relative to microtubule polarity, which is fixed through the tachyzoite life stage. MLC1 proteins were frequently immobile ('bound') for tens of seconds (Fig. 1b, Supplementary Fig. 2a and Supplementary Video 2), consistent with a stably anchored population of MyoA motors at the IMC. Relative to MLC1, a larger fraction of actin was mobile (Supplementary Fig. 2b) and displayed meandering ('diffusive') behaviour as well as ballistic
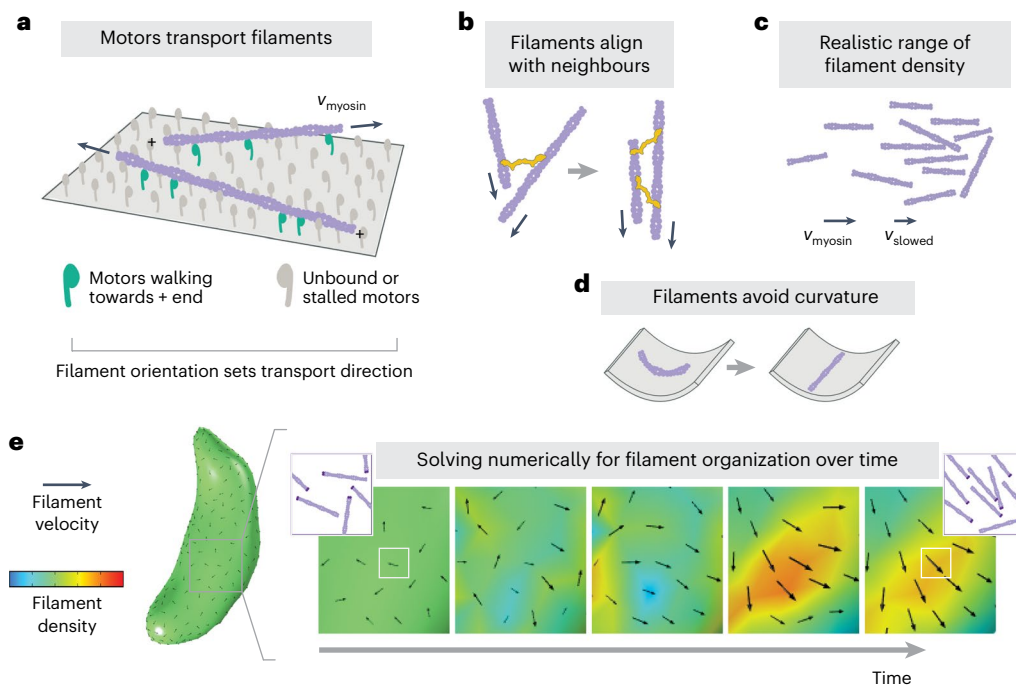
Fig. 2 | *Toxoplasma* actin self-organization: theoretical model. Rules of local actin filament behaviour, implemented in equation (2): **a**, Actin filaments (purple) are transported with their minus ends leading at speed v_{myosin}, as indicated by arrows. **b**, Neighbouring filaments align by steric effects or crosslinking proteins (yellow). **c**, Filament density remains within a realistic range, with filament speed slowing if entering a pile-up. **d**, Filament orientation is biased towards lower curvature. **e**, Example of numerically solving for filament self-organization using the finite element method, predicting filament density and velocity over time. Black arrow size reflects velocity magnitude. To provide intuition, for each white box, the corresponding inset shows schematized F-actin (darker purple represents minus ends) whose density and orientation are consistent with the simulation density (colour) and velocity (black arrow).

('directional') behaviour consistent with processive transport of filaments by myosin (Fig. 1c and Supplementary Video 3). Directional actin moved with a mean speed of 4.8 µm s^{-1} (Fig. 1d), similar to the in vitro actin transport speeds of 4–5 µm s^{-1} reported for purified *Toxoplasma* MyoA complexes[22,23].

Analysis of directional actin tracks in live parasites was inconsistent with a mechanistic model featuring fixed myosin polarity and uniformly rearward actin flow. Relative to the parasite long axis, F-actin transport direction was heterogeneous and as often forward as rearward (Fig. 1e,f). Although the orientation of subpellicular microtubules or IMC surface filaments could contribute to the observed bias towards longitudinal F-actin transport (Fig. 1f), for example by steric channelling[19] or by scaffolding closer longitudinal than latitudinal MyoA spacing[24], microtubule polarity evidently did not template rearward-only actin transport.

A theoretical model of actin filament collective motion

Our data, combined with the diversity of gliding modes exhibited by motile Apicomplexa, led us to explore the possibility that gliding motility might represent an emergent self-organized state rather than the consequence of a microtubule-templated asymmetry in actomyosin polarity. In this scenario, the heterogenous F-actin transport observed between glides (Fig. 1d–f) could reflect a disorganized state between transient self-organized actin states that drive gliding. Self-organization[25] is a hallmark of actomyosin networks, with morphologically diverse examples such as the lamellipodia of crawling keratocytes[26] and neutrophils[27], the flowing cortex of *C. elegans* zygotes[28], and dense actin networks of in vitro motility systems[29]. Drawing on continuum theories for active collective motion or flocking[30–32] and previous studies of self-organization of cytoskeletal systems[28,33,34], we developed a continuum model of *Toxoplasma* actin filament collective motion (Fig. 2 and Supplementary Fig. 3). In our model, actin filaments

at the surface of the cell follow a few simple rules: filaments are transported at the speed of myosin motors, and filament orientation sets the myosin-driven transport direction (Fig. 2a); filaments align with neighbouring filaments through collisions[35] or due to crosslinking proteins like *Toxoplasma* coronin[36–38] (Fig. 2b); filament density remains within a realistic range (Fig. 2c); and filament alignment is biased away from orientations of high membrane curvature (Fig. 2d). Actin filament organization over space and time (t) is described by two fields: the scalar field ρ, which captures filament density, and the velocity vector field **v**, which captures both filament polarity (orientation of **v**) and speed (magnitude of **v**). Two equations are needed: the continuity equation

$$\frac{\partial \rho}{\partial t} + \nabla \cdot (\rho \mathbf{v}) = 0 \qquad (1)$$

ensures conservation of filaments, and filament velocity evolves according to the rules described above using the minimal Toner–Tu equations

$$\frac{\partial \mathbf{v}}{\partial t} = -\lambda \mathbf{v} \cdot \nabla \mathbf{v} + \left(\alpha (\rho - \rho_c) - \beta |\mathbf{v}|^2 \right) \mathbf{v}$$
$$+ D\nabla^2 \mathbf{v} - \sigma \nabla \rho - \varepsilon F_K (\mathbf{v}, \kappa) (I - \hat{\mathbf{v}} \otimes \hat{\mathbf{v}}) \mathbf{d_1} \qquad (2)$$

where ρ_c is the critical density above which filaments move coherently, the coefficient λ tunes filament transport (self-advection), the ratio of α and β sets a filament transport speed scale, D tunes filament alignment with neighbours, $\sigma \nabla \rho$ provides an effective pressure that limits density variance, $\hat{\mathbf{v}}$ is a unit vector in direction **v**, I is the identity matrix, and the coefficient ε tunes the curvature (κ)-induced force $F_K(\mathbf{v}, \kappa)$ that rotates filaments away from $\mathbf{d_1}$, the direction of maximum curvature (Supplementary Fig. 3). This final term generally favours filament alignment to the cell long axis and could also capture, conceptually, an orientation bias from the subpellicular microtubules or IMC
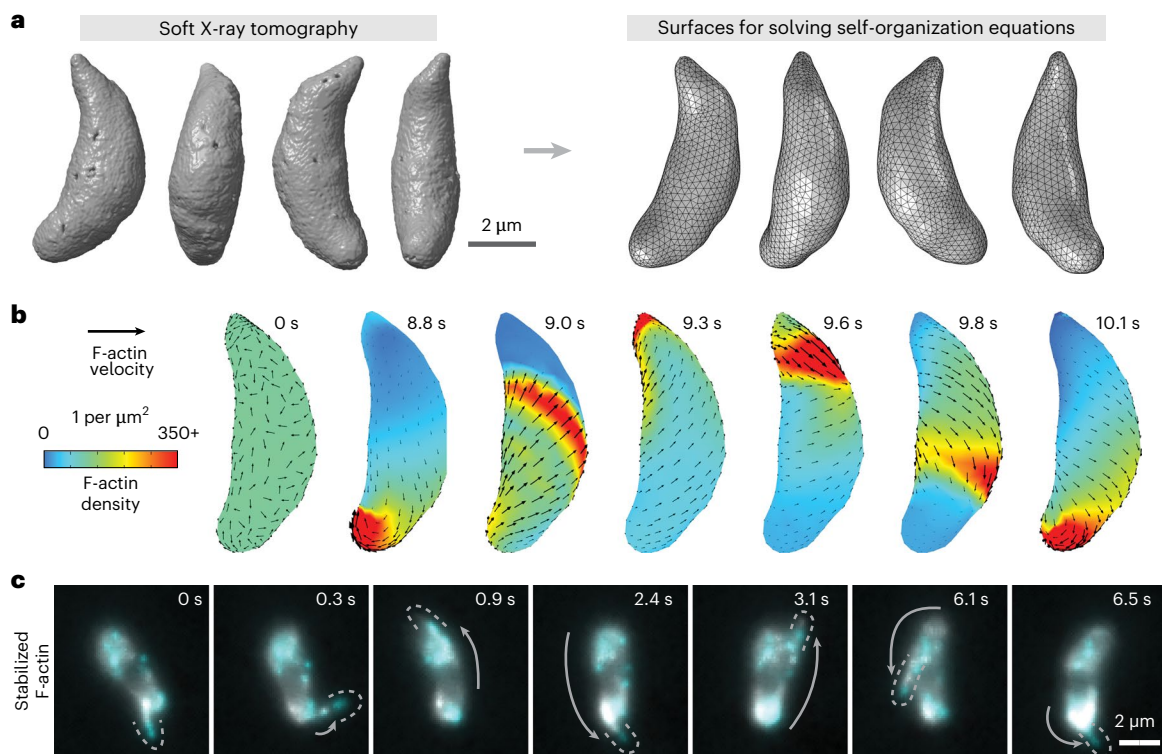
Fig. 3 | Stable actin filaments circle the *Toxoplasma* cell. a, Soft X-ray tomograms of cryo-fixed extracellular *Toxoplasma gondii* tachyzoites were used to generate triangle-meshed surfaces on which to solve our actin self-organization theoretical model. **b**, For stable filaments, solving the model constrained to *Toxoplasma*'s surface geometry predicts recirculating actin patches. **c**, In experiments, actin filaments briefly stabilized with jasplakinolide can circle around the cell. Cyan and grey both show actin, labelled at different dye densities. Images denoised with noise2void[60]. Dotted lines outline protruding actin filaments, and grey arrows highlight the movement of the protrusion since the previous frame. Representative of *n* = 10 cells whose protrusion velocities are characterized in Supplementary Fig. 4.

surface filaments[19]. The exclusion of any of these terms leads to results that are either unphysical or inconsistent with established *Toxoplasma* biology (Supplementary Information Section 6). Although likely a simplification, the generality of this minimal flocking framework allowed us to explore how cell-scale actin organization might emerge from local actomyosin interactions confined to *Toxoplasma*'s surface shape.

To predict what cell-scale actin organization patterns could emerge from the molecule-scale rules illustrated in Fig. 2, we began with a disordered network and asked how filament density and velocity evolve over time (Fig. 2e), using the finite element method to solve equations (1) and (2) in COMSOL Multiphysics. Importantly, we sought to incorporate the true shape of this thin membrane-constrained layer of actin, which can be approximated as a two-dimensional closed surface following the rigid and stereotypical shape of *Toxoplasma gondii* tachyzoites. We used soft X-ray tomography[39] to obtain native-state high-resolution 3D reconstructions of cryo-fixed extracellular parasites and used a spherical harmonic description[40] to convert them to closed surfaces for finite element analysis (Fig. 3a). We then derived a curved-surface formulation of our governing equations (1) and (2) using extrinsic differential geometry[41–43] (Supplementary Information Section 8). In essence, the resulting formulation uses the surface normal vector to project into the local tangent plane and thus requires no intrinsic surface parameterization. We note the versatility of such an approach for solving continuum models on complex geometries for both living and non-living systems[42,44].

A transition from recirculation to unidirectional actin transport

Starting from a disordered initial state and, importantly, the assumption of a conserved number of stable actin filaments enforced by

equation (1), numerical simulations predicted the emergence of patches of parallel actin filaments that circulate up and down along the cell as shown in Fig. 3b and Supplementary Video 4. We observed a similar recirculation of F-actin in experiments, imaging actin bundles in *Toxoplasma* tachyzoites treated briefly with the actin-stabilizing drug jasplakinolide (Fig. 3c and Supplementary Video 5). Actin bundles repeatedly circled the cell at a mean speed of 5.7 µm s^{-1} ± 3.2 s.d. (Supplementary Fig. 4). Thus, in the absence of filament turnover, a self-organization model predicts the emergence of F-actin recirculation: a continuous 'cyclosis' observed experimentally for stabilized filaments in live parasites.

Next, we extended these theoretical and experimental results to consider regimes of filament turnover. Importantly, *Toxoplasma* helical and circular gliding modes are known to require regulated actin depolymerization by proteins like profilin[45] and actin depolymerizing factor (ADF)[46]. Further, the polymerization of F-actin essential to gliding depends on formin 1 (FRM1), which localizes to the parasite anterior[47–49]. Estimates of F-actin lifetime and the characteristic timescale of F-actin cyclosis are both on the order of seconds, justifying an addition of filament turnover to our theoretical model that extends it beyond prior flocking models[50] (Supplementary Information Section 6.4). Based on current knowledge, polymerization is favoured specifically at the cell anterior, whereas depolymerization by profilin and ADF is not known to be spatially restricted. Thus, in the filament turnover model, F-actin density at the anterior cell surface is governed by

$$\frac{\partial \rho}{\partial t} + \nabla \cdot (\rho \mathbf{v}) = c - \gamma \rho \tag{3}$$

where *c* tunes F-actin polymerization and stabilization (rate of filaments produced per unit area) and *γ* tunes depolymerization (rate of
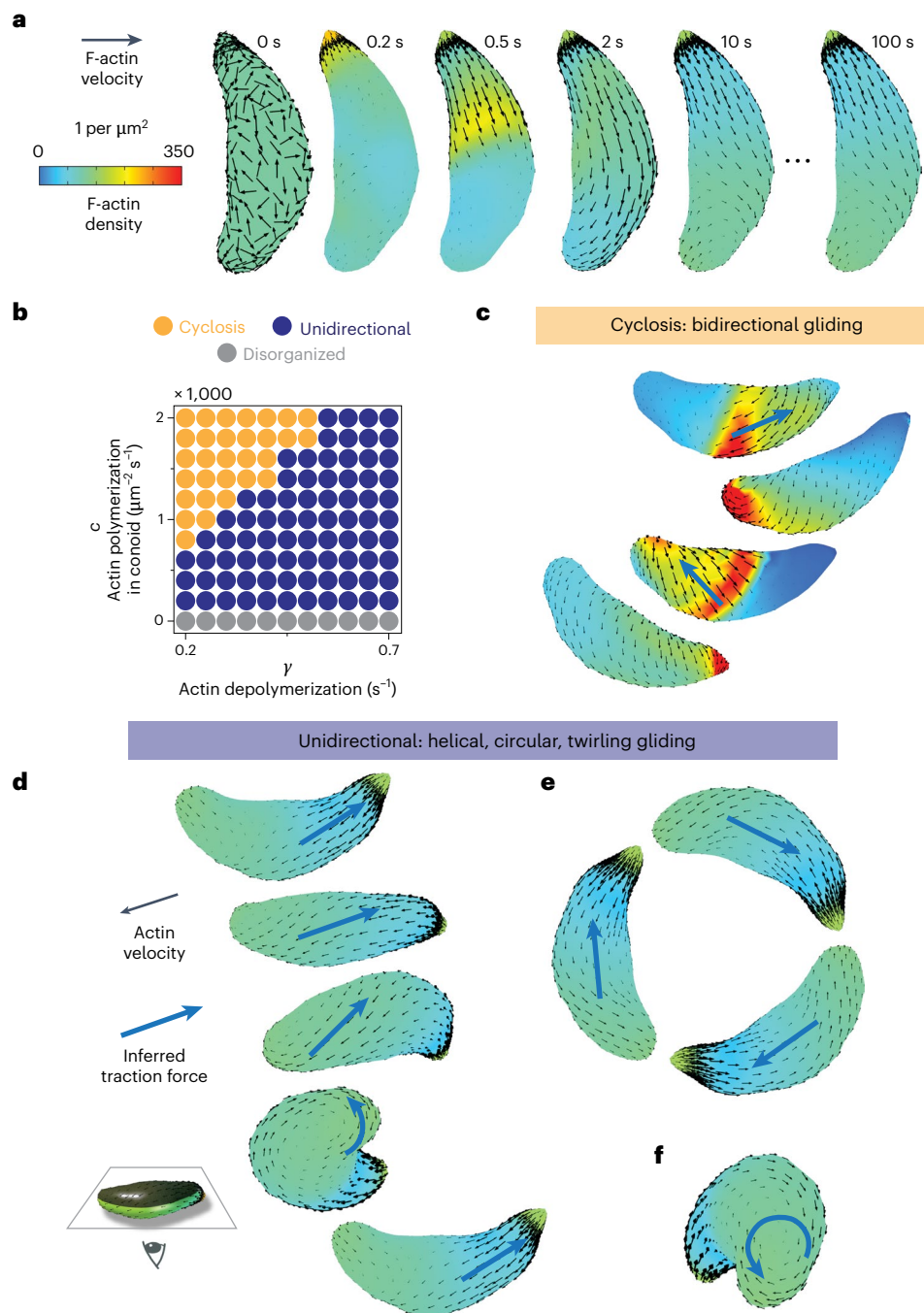
Fig. 4 | Polarized actin turnover governs a transition between actin recirculation and unidirectional transport. a, Incorporating F-actin depolymerization and anterior polymerization into the model enables the emergence of a unidirectional, stable velocity pattern. **b**, Tuning rates of F-actin polymerization and depolymerization move the cell between distinct self-organized states: bidirectional cyclosis, unidirectional and disorganized. **c**, Model prediction: recirculating F-actin cyclosis generates bidirectional traction force (blue arrows) to drive 'patch' gliding. **d**–**f**, Model prediction: the unidirectional self-organized F-actin state drives helical gliding (**d**), circular gliding (**e**) and twirling (**f**). In the images in **c**–**f**, cells are viewed from below; cell-substrate contact occurs at the position of the inferred traction force.

filament loss). Outside the cell anterior (Supplementary Fig. 4), F-actin density is governed by

$$\frac{\partial \rho}{\partial t} + \nabla \cdot (\rho \mathbf{v}) = -\gamma \rho \tag{4}$$

while F-actin velocity across the entirety of the cell is governed by equation (2).

The addition of F-actin turnover and anterior polymerization enabled the emergence of a new F-actin organization state, in which actin transport is largely unidirectional and rearward (Fig. 4a and Supplementary Video 6). In this emergent state, filament density and velocity reach a steady state: whereas individual actin filaments flow continuously rearward, the average F-actin density and velocity at a given position reaches a fixed value. The asymmetric *Toxoplasma* cell shape was necessary for the emergence of this steady state and its consistent chirality (Supplementary Fig. 5). Tuning filament polymerization and depolymerization rates (Fig. 4b) shifted the emergent F-actin pattern between states. Increasing anterior polymerization and increasing filament stability (lowering depolymerization rate) favoured

the F-actin cyclosis described in Fig. 3. Conversely, increasing filament depolymerization rate favoured unidirectional F-actin transport. At an intuitive level, the transition from cyclosis to unidirectional flow occurs as filament lifetime ($1/\gamma$) drops below the cross-cell filament transport time ($\sim L_{cell}/v_{myosin}$), preventing a posterior pile-up of F-actin large enough to force recirculation. In summary, actin turnover governs a transition between two self-organized states: F-actin recirculation and steady-state unidirectional transport.

Self-organized actin states can account for gliding behaviours

In this section, we develop the working hypothesis that actin self-organization into distinct states explains the rich diversity of apicomplexan cell movements observed experimentally, from helical gliding and twirling to back-and-forth patch gliding[5,11,51]. During gliding on a surface, parasites form an adhesive cell-substrate contact point, where adhesin proteins bind the external substrate and form a stationary patch[48,52]. Cell motion occurs when MyoA walks the inner cytoskeleton and parasite cytoplasm towards the plus ends of F-actin adhering to that stationary patch[9,22]. Therefore, local F-actin polarity dictates the direction of myosin-powered traction force and the direction of cell movement (Supplementary Fig. 6). A map of self-organized actin velocity (Figs. 3b and 4a) thus implies a corresponding map of traction force direction (blue arrows, Fig. 4c–e).

In the recirculating actin state, a qualitative translation of predicted F-actin velocity patterns into traction force orientation (blue arrows, Fig. 4c) can explain the previously puzzling observations of back-and-forth *Toxoplasma* and *Plasmodium* cell gliding summarized in Supplementary Table 1. These observations include patch gliding, pendulum gliding and rolling in conditions like *Toxoplasma gondii* actin depolymerization factor (ADF) knockout cells[46], *Toxoplasma gondii* treated with actin stabilizers[5] and *Plasmodium berghei* sporozoites with mutations in the actin-binding adhesin protein TRAP[51,53] or in actin itself[54,55]. Our theoretical finding that increased filament stability shifts F-actin self-organization from a unidirectional to recirculating mode (Fig. 4b) provides a unifying interpretation of these disparate experimental results (Supplementary Table 1).

In the unidirectional regime, tuning the rate of F-actin depolymerization changes features of the predicted velocity patterns, including chirality and density gradient length scale (Supplementary Fig. 7). For choices of polymerization and depolymerization rate close to the unidirectional-to-recirculating transition, emergent F-actin velocity patterns are consistent with the observed mechanics of helical gliding, circular gliding and twirling (Fig. 4d–f). Helical gliding initiates when the 'left' side of the cell is in contact with the substrate, whereas circular gliding initiates given 'right' side contact (considering the concave cell surface to be ventral)[11]. In each case, inferred traction force vectors along the path of substrate contact can qualitatively explain observed cell translation and rotation (Fig. 4d,e). Similarly, predicted vortical F-actin polarity at the parasite posterior would lead to a myosin-powered torque and cell rotation or twirling, which is indeed characteristic during cell posterior contact (Fig. 4f). Thus, we hypothesize that the cyclosis mode of F-actin self-organization (Figs. 3b and 4c) drives bidirectional cell gliding (patch, pendulum, rolling); the unidirectional mode of F-actin self-organization (Fig. 4a,d–f) drives helical gliding, circular gliding and twirling; and actin turnover governs the transition between modes. Indeed, decreasing F-actin turnover through titrated jasplakinolide treatment led to more frequent bidirectional gliding and less unidirectional gliding (Supplementary Fig. 8a) but did not change the fractional breakdown of unidirectional gliding into helical, circular and twirling movements (Supplementary Fig. 8b).

We hope that the theoretical and experimental results presented here will prove a stimulating first step in understanding actomyosin self-organization in the Apicomplexa, given the fruitfulness of the self-organization paradigm as a null hypothesis for cytoskeletal systems across biology. Far from wishing to claim finality for the particulars of the model developed here, we look forward to the incorporation and discovery of additional biological complexity through a dialogue between theory and experiment. Such a dialogue will benefit from fast and sensitive volumetric imaging of actin single molecules, combined with sufficiently sophisticated analysis algorithms, to enable 3D reconstructions of F-actin velocity fields in the reference frame of the cell during specific gliding motions and from quantitative comparison of predicted and measured traction forces and gliding mechanics[51,52,56].

Broadly, we note continuum theory's ability to unify natural phenomena across scales, allowing a flocking theory inspired by collective bird motion[30,32] to provide insight into microscopic actin organization in a unicellular parasite. Looking forward, the mathematical framework developed here will enable a meaningful examination of actomyosin self-organization in *Plasmodium* spp. sporozoites, ookinetes and other motile Apicomplexa, incorporating their characteristic cell shapes to generate self-organized patterns of actin velocity and inferred traction force for comparison to experimental data. Further, reports of gliding cells exist within at least three major clades of eukaryotic life[57,58], suggesting that this 'esoteric' mode of cell locomotion may in fact be common but understudied and deserving of a unifying effort[59] to understand its physical principles and their degree of conservation across Eukarya.

Online content

Any methods, additional references, Nature Portfolio reporting summaries, source data, extended data, supplementary information, acknowledgements, peer review information; details of author contributions and competing interests; and statements of data and code availability are available at https://doi.org/10.1038/s41567-024-02652-4.

References

1. Tenter, A. M., Heckeroth, A. R. & Weiss, L. M. *Toxoplasma gondii*: from animals to humans. *Int. J. Parasitol.* **30**, 1217–1258 (2000).
2. Checkley, W. et al. A review of the global burden, novel diagnostics, therapeutics, and vaccine targets for *cryptosporidium*. *Lancet Infect. Dis.* **15**, 85–94 (2015).
3. White, N. J. et al. Malaria. *Lancet* **383**, 723–735 (2014).
4. Jensen, J. B. & Edgar, S. A. Effects of antiphagocytic agents on penetration of *Eimeria magna* sporozoites into cultured cells. *J. Parasitol.* **62**, 203–206 (1976).
5. Wetzel, D. M., Håkansson, S., Hu, K., Roos, D. & Sibley, L. D. Actin filament polymerization regulates gliding motility by apicomplexan parasites. *Mol. Biol. Cell* **14**, 396–406 (2003).
6. Meissner, M., Schlüter, D. & Soldati, D. Role of *Toxoplasma gondii* myosin A in powering parasite gliding and host cell invasion. *Science* **298**, 837–840 (2002).
7. Frénal, K. et al. Functional dissection of the apicomplexan glideosome molecular architecture. *Cell Host Microbe* **8**, 343–357 (2010).
8. Gaskins, E. et al. Identification of the membrane receptor of a class XIV myosin in *Toxoplasma gondii*. *J. Cell Biol.* **165**, 383–393 (2004).
9. Frénal, K., Dubremetz, J. F., Lebrun, M. & Soldati-Favre, D. Gliding motility powers invasion and egress in Apicomplexa. *Nat. Rev. Microbiol.* **15**, 645–660 (2017).
10. Tardieux, I. & Baum, J. Reassessing the mechanics of parasite motility and host-cell invasion. *J. Cell Biol.* **214**, 507–515 (2016).
11. Håkansson, S., Morisaki, H., Heuser, J. & Sibley, L. D. Time-lapse video microscopy of gliding motility in *Toxoplasma gondii* reveals a novel, biphasic mechanism of cell locomotion. *Mol. Biol. Cell* **10**, 3539–3547 (1999).

12. Leung, J. M., Rould, M. A., Konradt, C., Hunter, C. A. & Ward, G. E. Disruption of TgPHIL1 alters specific parameters of *Toxoplasma gondii* motility measured in a quantitative, three-dimensional live motility assay. *PLoS ONE* **9**, e85763 (2014).

13. Akaki, M. & Dvorak, J. A. A chemotactic response facilitates mosquito salivary gland infection by malaria sporozoites. *J. Exp. Biol.* **208**, 3211–3218 (2005).

14. Kan, A. et al. Quantitative analysis of *Plasmodium* ookinete motion in three dimensions suggests a critical role for cell shape in the biomechanics of malaria parasite gliding motility. *Cell. Microbiol.* **16**, 734–750 (2014).

15. Graindorge, A. et al. The conoid associated motor MyoH Is indispensable for *Toxoplasma gondii* entry and exit from host cells. *PLoS Pathog.* **12**, e1005388 (2016).

16. Bergman, L. W. et al. Myosin A tail domain interacting protein (MTIP) localizes to the inner membrane complex of *Plasmodium* sporozoites. *J. Cell Sci.* **116**, 39–49 (2003).

17. Tengganu, I. F. et al. The cortical microtubules of *Toxoplasma gondii* underlie the helicity of parasite movement. *J. Cell Sci.* **136**, jcs261270 (2023).

18. Yahata, K. et al. Gliding motility of *Plasmodium* merozoites. *Proc. Natl Acad. Sci. USA* **118**, e2114442118 (2021).

19. Martinez, M. et al. Origin and arrangement of actin filaments for gliding motility in apicomplexan parasites revealed by cryo-electron tomography. *Nat. Commun.* **14**, 4800 (2023).

20. Grimm, J. B. et al. A general method to improve fluorophores for live-cell and single-molecule microscopy. *Nat. Methods* **12**, 244–250 (2015).

21. Miller, C. M., Korkmazhan, E. & Dunn, A. R. Extraction of accurate cytoskeletal actin velocity distributions from noisy measurements. *Nat. Commun.* **13**, 4749 (2022).

22. Herm-Götz, A. et al. *Toxoplasma gondii* myosin A and its light chain: a fast, single-headed, plus-end-directed motor. *EMBO J.* **21**, 2149–2158 (2002).

23. Heaslip, A. T. et al. A small-molecule inhibitor of *T. gondii* motility induces the posttranslational modification of myosin light chain-1 and inhibits myosin motor activity. *PLoS Pathog.* **6**, e1000720 (2010).

24. Stadler, R. V., White, L. A., Hu, K., Helmke, B. P. & Guilford, W. H. Direct measurement of cortical force generation and polarization in a living parasite. *Mol. Biol. Cell* **28**, 1912–1923 (2017).

25. Karsenti, E. Self-organization in cell biology: a brief history. *Nat. Rev. Mol. Cell Biol.* **9**, 255–262 (2008).

26. Yam, P. T. et al. Actin-myosin network reorganization breaks symmetry at the cell rear to spontaneously initiate polarized cell motility. *J. Cell Biol.* **178**, 1207–1221 (2007).

27. Xu, J. et al. Divergent signals and cytoskeletal assemblies regulate self-organizing polarity in neutrophils. *Cell* **114**, 201–214 (2003).

28. Mayer, M., Depken, M., Bois, J. S., Jülicher, F. & Grill, S. W. Anisotropies in cortical tension reveal the physical basis of polarizing cortical flows. *Nature* **467**, 617–621 (2010).

29. Schaller, V., Weber, C., Semmrich, C., Frey, E. & Bausch, A. R. Polar patterns of driven filaments. *Nature* **467**, 73–77 (2010).

30. Toner, J. & Tu, Y. Long-range order in a two-dimensional dynamical XY model: how birds fly together. *Phys. Rev. Lett.* **75**, 4326–4329 (1995).

31. Vicsek, T., Czirók, A., Ben-Jacob, E., Cohen, I. & Shochet, O. Novel type of phase transition in a system of self-driven particles. *Phys. Rev. Lett.* **75**, 1226–1229 (1995).

32. Toner, J. & Tu, Y. Flocks, herds, and schools: a quantitative theory of flocking. *Phys. Rev. E* **58**, 4828–4858 (1998).

33. Woodhouse, F. G. & Goldstein, R. E. Cytoplasmic streaming in plant cells emerges naturally by microfilament self-organization. *Proc. Natl Acad. Sci. USA* **110**, 14132–14137 (2013).

34. Shankar, S., Bowick, M. J. & Marchetti, M. C. Topological sound and flocking on curved surfaces. *Phys. Rev. X* **7**, 031039 (2017).

35. Sciortino, A. & Bausch, A. R. Pattern formation and polarity sorting of driven actin filaments on lipid membranes. *Proc. Natl Acad. Sci. USA* **118**, e2017047118 (2021).

36. Salamun, J., Kallio, J. P., Daher, W., Soldati-Favre, D. & Kursula, I. Structure of *Toxoplasma gondii* coronin, an actin-binding protein that relocalizes to the posterior pole of invasive parasites and contributes to invasion and egress. *FASEB J.* **28**, 4729–4747 (2014).

37. Olshina, M. A. et al. *Plasmodium falciparum* coronin organizes arrays of parallel actin filaments potentially guiding directional motility in invasive malaria parasites. *Malar. J.* **14**, 280 (2015).

38. Bane, K. S. et al. The actin filament-binding protein coronin regulates motility in *Plasmodium* sporozoites. *PLoS Pathog.* **12**, e1005710 (2016).

39. Guo, J. & Larabell, C. A. Soft X-ray tomography: virtual sculptures from cell cultures. *Curr. Opin. Struct. Biol.* **58**, 324–332 (2019).

40. Styner, M. et al. Framework for the statistical shape analysis of brain structures using SPHARM-PDM. *Insight J.* **1071**, 242–250 (2006).

41. Jankuhn, T., Olshanskii, M. A. & Reusken, A. Incompressible fluid problems on embedded surfaces: modeling and variational formulations. *Interface Free Bound.* **20**, 353–378 (2018).

42. Hueschen, C. L., Dunn, A. R. & Phillips, R. Wildebeest herds on rolling hills: flocking on arbitrary curved surfaces. *Phys. Rev. E* **108**, 24610 (2023).

43. Needham, T. *Visual Differential Geometry and Forms: A Mathematical Drama in Five Acts* (Princeton Univ. Press, 2021).

44. Hueschen, C. & Phillips, R. *The Restless Cell: Continuum Theories of Living Matter* (Princeton Univ. Press, 2024).

45. Plattner, F. et al. *Toxoplasma* profilin is essential for host cell invasion and TLR11-dependent induction of an interleukin-12 response. *Cell Host Microbe* **3**, 77–87 (2008).

46. Mehta, S. & Sibley, L. D. Actin depolymerizing factor controls actin turnover and gliding motility in *Toxoplasma gondii*. *Mol. Biol. Cell* **22**, 1290–1299 (2011).

47. Baum, J. et al. A malaria parasite formin regulates actin polymerization and localizes to the parasite-erythrocyte moving junction during invasion. *Cell Host Microbe* **3**, 188–198 (2008).

48. Tosetti, N., Pacheco, N. D. S., Favre, D. S. & Jacot, D. Three F-actin assembly centers regulate organelle inheritance, cell-cell communication and motility in *Toxoplasma gondii*. *eLife* **8**, e42669 (2019).

49. Dos Santos Pacheco, N. et al. Conoid extrusion regulates glideosome assembly to control motility and invasion in Apicomplexa. *Nat. Microbiol.* **7**, 1777–1790 (2022).

50. Marchetti, M. C. et al. Hydrodynamics of soft active matter. *Rev. Mod. Phys.* **85**, 1143–1189 (2013).

51. Münter, S. et al. *Plasmodium* sporozoite motility is modulated by the turnover of discrete adhesion sites. *Cell Host Microbe* **6**, 551–562 (2009).

52. Pavlou, G. et al. Coupling polar adhesion with traction, spring, and torque forces allows high-speed helical migration of the protozoan parasite. *Toxoplasma. ACS Nano* **14**, 7121–7139 (2020).

53. Kappe, S. et al. Conservation of a gliding motility and cell invasion machinery in Apicomplexan parasites. *J. Cell Biol.* **147**, 937–944 (1999).

54. Douglas, R. G. et al. Inter-subunit interactions drive divergent dynamics in mammalian and *Plasmodium* actin filaments. *PLoS Biol.* **16**, e2005345 (2018).

55. Yee, M., Walther, T., Frischknecht, F. & Douglas, R. G. Divergent *Plasmodium* actin residues are essential for filament localization, mosquito salivary gland invasion and malaria transmission. *PLoS Pathog.* **18**, e1010779 (2022).

56. Stadler, R. V., Nelson, S. R., Warshaw, D. M. & Ward, G. E. A circular zone of attachment to the extracellular matrix provides directionality to the motility of *Toxoplasma gondii* in 3D. *eLife* **11**, e85171 (2022).

57. Keeling, P. J. et al. The Marine Microbial Eukaryote Transcriptome Sequencing Project (MMETSP): illuminating the functional diversity of eukaryotic life in the oceans through transcriptome sequencing. *PLoS Biol.* **12**, e1001889 (2014).

58. Häder, D. P. & Hoiczyk, E. in *Algal Cell Motility* (ed. Melkonian, M.) Ch. 1 (Springer, 1992).

59. Lettermann, L., Ziebert, F. & Schwarz, U. S. A geometrical theory of gliding motility based on cell shape and surface flow. *Proc. Natl Acad. Sci. USA* **121**, e2410708121 (2024).

60. Krull, A., Buchholz, T.-O. & Jug, F. Noise2Void – learning denoising from single noisy images. In *Proc. IEEE/CVF Conference on Computer Vision and Pattern Recognition* 2124–2132 (2019).

Methods

Parasite and host cell culture

Toxoplasma gondii type I RH tachyzoites were maintained by serial passage in primary human foreskin fibroblasts (HFFs) in Dulbeccos modified Eagles high glucose medium (DMEM; Gibco 11960-044) with 10% heat-inactivated foetal bovine serum (FBS; Corning 35-011-CV), 2 mM glutamine (Sigma-Aldrich G7513), 100 U ml^{-1} penicillin and 100 µg ml^{-1} streptomycin (Gibco 15140122) at 37 °C in 5% CO_2. In brief, to passage parasites, infected HFF monolayers were suspended in media by scraping, syringe lysed using a 25-gauge blunt-end needle (SAI Technologies B25-50) and added at a 150-fold dilution to an confluent uninfected HFF monolayer, every 2–4 days. HFFs were obtained from the neonatal clinic at Stanford University following routine circumcisions that are performed at the request of the parents for cultural, health or other personal medical reasons (that is, not in any way related to research). These foreskins, which would otherwise be discarded, were fully deidentified and therefore do not constitute human subjects research. Uninfected HFFs were maintained in the supplemented DMEM described above, passaged using 0.25% trypsin-EDTA (Gibco 25200056) and discarded after passage 15.

Generation of halo-ACT1 and MLC1-halo strains

In brief, halo-TgACT1 or TgMLC1-halo fusions under the control of a weak promoter (from TGGT1 239010, gift of M. Panas[61]) were incorporated into the genome of the *Toxoplasma gondii* type I RH Δhxgprt Δku80 strain[62]. In detail, p239010-halo-C1-HXGPRT and p239010-halo-N1-HXGPRT vectors were created by replacing a region of the pGRA-3xHA-HPT vector[63] (from the pGRA promoter through the translated region) with (1) the TGGT1 239010 promoter and 5′ UTR to drive low expression levels, (2) the HaloTag sequence (Promega) and (3) a serine-glycine linker and multiple cloning site either C-terminal ('C1') or N-terminal ('N1') to the HaloTag sequence. TgACT1 (TGGT1 209030) or TgMLC1 (TGGT1 257680) was then synthesized and cloned into the p239010-halo-C1-HXGPRT or p239010-halo-N1-HXGPRT vector, respectively (Epoch Life Science, Inc.). For transfection with p239010-halo-ACT1-HXGPRT or p239010-MLC1-halo-HXGPRT, RH Δhxgprt Δku80 parasites were mechanically released in phosphate-buffered saline (PBS), pelleted and resuspended in 20 µl P3 primary cell Nucleofector solution (Lonza) with 15 µg DNA and electroporated using the Amaxa 4D Nucleofector (Lonza). Transfected parasites were permitted to infect and grow in confluent HFFs for 48 h, after which time the media was supplemented with 50 µg ml^{-1} mycophenolic acid and 50 µg ml^{-1} xanthine for HXGPRT selection. Parasites were passaged four times over 10–12 days in selection media before being singly cloned into 96-well plates by limiting dilution. Clones were expanded and screened for HaloTag expression by incubating intracellular parasites overnight with 50 nM TMR HaloTag Ligand (Promega G8251), washing 5× with PBS to remove unbound dye, fixing with 4% paraformaldehyde (EMS AA433689M) for 15 min and imaging fluorescence.

Single-molecule (speckle) and bulk labelling in live parasites

Before infected HFFs were lysed to release parasites for imaging, parasites within infected HFF monolayers were labelled for 3 h at 37 °C with Janelia Fluor 549 HaloTag Ligand (Promega GA1110) and Janelia Fluor 646 HaloTag Ligand (Promega GA1120)[20] at a concentration of 1–10 pM for single-molecule imaging or 100–500 pM for bulk population imaging. For example, the MLC1-halo parasites shown in Fig. 1 show MLC1 labelled with 10 pM (cyan speckles) and at 200 pM (magenta bulk population of MLC1, showing the shape of the cell). Because Janelia Fluor dyes bleach over time in storage, dye concentration must be optimized empirically and adjusted on the timescale of months; furthermore, care should be taken to avoid more than two or three freeze–thaw cycles before use. When subpellicular microtubule imaging was used to determine parasite polarity, infected HFFs were

labelled with 100 nM siR-tubulin and 10 µM verapamil (Cytoskeleton, Inc. CY-SC002) alongside 1–10 pM Janelia Fluor 549. Before parasite release, infected HFF monolayers were washed 7× with DMEM to ensure removal of unbound dye.

Preparation and TIRF imaging of live extracellular parasites

To release parasites, infected HFFs were scraped and syringe lysed in fresh phenol red-free DMEM with a 27-gauge needle (SAI Technologies B27-50). Freshly released parasites were placed on 35 mm #1.5 glass-bottomed dishes (Cellvis D35-20-1.5-N; incubated with 10% FBS before use) with a confluent monolayer of HFFs grown on Snapwell Insert polyester membranes (Corning Costar CLS3801) suspended approximately 0.2 mm above them. Parasites were imaged at 30 °C using objective-type total internal reflection fluorescence (TIRF) microscopy on an inverted microscope (Nikon Ti-E) with a heated Apo TIRF 100 oil objective of numerical aperture 1.49 (Nikon) and controlled using Micro-Manager v.1.4 (ref. 64). To enable simultaneous two-colour imaging, samples were excited with both 532 nm (Crystalaser) and 635 nm (Blue Sky Research) lasers and emitted light passed through a quad-edge laser-flat dichroic with centre/bandwidths of 405 nm/60 nm, 488 nm/100 nm, 532 nm/100 nm and 635 nm/100 nm from Semrock (Di01-R405/488/532/635-25×36) and corresponding quad-pass filter with centre/bandwidths of 446 nm/30 nm, 510 nm/30 nm, 581 nm/30 nm, 703 nm/30 nm band-pass filter (FF01-446/510/581/703-25). Emission channels were then separated as previously described[65] and recorded on an electron-multiplying charge-coupled device camera (Andor iXon).

Frequency of gliding modes with titrated actin stabilization by jasplakinolide (low concentrations)

Live extracellular parasites were prepared as in the preceding section and added to microgrids of 75 µm × 75 µm square PDMS wells (Microsurfaces MGA-075-02) in glass-bottomed 24-well plates. Upon addition of 650,000 parasites per well, plates were spun at 100 g for 3 min to settled parasites into grids. For jasplakinolide experiments, the indicated concentrations (Supplementary Fig. 8) of jasplakinolide (Millipore Sigma J4580) were then added and mixed by pipetting. Imaging began 40–50 min later. Multiple stage positions were imaged per condition, and microgrid walls prevented shear stress or parasite detachment from sloshing of imaging media. Brightfield images were acquired at a frame rate of five frames per second at 37 °C in 5% CO_2 using a Nikon Ti-E inverted microscope with a 20×/0.5 numerical aperture Plan Fluor CFI air objective and an Andor Neo camera. Image acquisition was controlled using Micro-Manager software[64].

For the fraction of cells in each motility mode reported in Supplementary Fig. 8, means were calculated by 'pooling' all measurements of motility events from three independent experiments. This is equivalent to a weighted mean, $x^* = \sum w_i x_i / \sum w_i$, where for experiment i the weight w_i is the total number of motility events measured and x_i is the fraction of cells in a given mode. Weighted standard deviations are calculated as $\sum w_i (x_i - x^*)^2 / \left(\sum w_i - \frac{\sum w_i^2}{\sum w_i} \right)$, where the denominator is a correction to yield an unbiased estimator given 'reliability' weights[66].

Jasplakinolide treatment (high concentration) and recirculating actin bundles

Live extracellular parasites were prepared as above, with the addition of 1 µM jasplakinolide (Millipore Sigma J4580) immediately before imaging. In a narrow window of time from approximately 15 min until 30 min after jasplakinolide addition, protruding bundles of actin filaments were observed circling around the periphery of parasites (Supplementary Fig. 4). We note that this recirculating behaviour was very sensitive to treatment time and drug concentration. Over time, most protrusions lost this recirculating behaviour and became fixed in position at the anterior (apical) end, as previously observed[67].

We speculate that this transition to fixed apical actin bundles occurs as bundles grow long enough (with polymerization favoured both by jasplakinolide and by apically-localized formin 1 (ref. [68])) to protrude through the conoid and into the cytoplasm and can no longer re-orient to contact myosin motors on the outside of the IMC. Under ideal treatment conditions, most extracellular parasites observed displayed recirculating actin protrusions; under less ideal conditions (for example, after more than 30 min treatment or with poorly attached parasites), less than 10% of parasites displayed recirculating protrusions. We also note that to image these large recirculating bundles, we relaxed the steep angle of the excitation light and performed highly inclined and laminated optical sheet (HILO) or 'dirty TIRF' imaging. Thus, fluorescently labelled actin structures within the cell cytoplasm are visible in addition to the gliding-associated surface actin.

MLC1 immunofluorescence and confocal microscopy

Parasites were released from infected HFF monolayers by scraping and syringe lysis in DMEM with a 27-gauge needle (SAI Technologies B27-50), passed through a 5 μm filter (Millipore Sigma SLSV025LS) and allowed to settle onto #1.5 coverslips at 37 °C in 5% CO_2 for 30 min in DMEM + 1 μM calcium ionophore A23187 (Sigma C7522). Subsequent staining steps were performed at room temperature: parasites were fixed with warm 4% paraformaldehyde (EMS AA433689M) for 15 min, washed 3× with PBS, incubated with permeabilization-and-blocking buffer (0.1% Triton-X-100 and 2% bovine serum albumin in PBS) for 20 min, incubated with mouse anti-tubulin monoclonal antibody DM1α (Sigma T6199; diluted 1:500) and 2 nM Janelia Fluor 646 HaloTag Ligand (Promega GA1120) in permeabilization-and-blocking buffer for 1 h, washed 3× with PBS, incubated with anti-mouse IgG secondary antibody conjugated to Alexa Fluor 488 (Cell Signaling 4408S, diluted 1:500) for 20 min, washed 3× with PBS and mounted in ProLong Gold Antifade (ThermoFisher P36934). Samples were imaged using an inverted Zeiss LSM 780 confocal microscope with a 63X/1.4 numerical aperture oil objective, 488 nm Ar laser, 633 nm HeNe laser and Zeiss Airyscan detector (32-channel gallium arsenide phosphide photomultiplier tube (GaAsP-PMT) area detector), in which using each detector element as an individual pinhole combined with linear deconvolution achieves a spatial resolution below the diffraction limit[69]. All images were acquired using Zen v.2.3 (black edition) software (Carl Zeiss).

Soft X-ray tomography

HFF monolayers, 18–20 h after parasite infection, were washed 2× with Hanks balanced salt solution (Gibco 14175095) supplemented with 1 mM magnesium chloride, 1 mM calcium chloride, 10 mM sodium hydrogen carbonate and 20 mM HEPES, pH 7. HFFs were scraped and passed through a 27-gauge needle (SAI Technologies B27-50) to release parasites into fresh Hanks balanced salt solution at room temperature. Calcium ionophore A23187 (Sigma C7522) at a final concentration of 1 μM was added to the sample at room temperature for 10 min. Parasites were pelleted, excess liquid was aspirated, and parasites were resuspended in the remaining liquid (~25 μl) before loading into 5-μm-diameter glass capillaries. Parasites inside capillaries were then vitrified by fast plunge-freezing in 90 K liquid propane. Capillaries were imaged using the XM-2 cryo soft X-ray microscope at the National Center for X-Ray Tomography at the Advanced Light Source (Lawrence Berkeley Laboratories). The XM-2 is equipped with a micro zone plate with a spatial resolution of 60 nm, and the imaged capillary was in an atmosphere of helium gas stream cooled by liquid nitrogen. To have a full rotated tomographic dataset reconstructed, 92 projection images were taken with 2° increments. The exposure time of each projection varied between 200 and 450 ms, depending on the beam flux and the sample thickness. Projection images were normalized and aligned, and the tomographic reconstructions were calculated using iterative reconstruction methods in the AREC-3D package[70]. Additional information on the soft X-ray tomography method is available in ref. [71].

Image analysis

Speckle tracking of actin and MLC1 was done using u-track software (v.2.2.0) made available by the Danuser lab[72] and run through MATLAB R2019a from Mathworks, Inc or by manual spot tracking of raw images with the Manual Tracking plugin[73] within Fiji (ImageJ v.0.0-rc-69/1.52p)[74]. Full analysis details and analysis methods for Supplementary Figs. 1, 2, 4 and 8 are presented in Supplementary Information Section 4.

Theoretical model of *Toxoplasma gondii* actin filament self-organization

To describe the collective motion and organization of actin filaments, we repurposed a classic continuum active matter model that was originally developed by John Toner and Yuhai Tu, inspired by the work of Tàmas Vicsek, to describe the collective behaviour of flocking or schooling animals[30–32]. This class of theoretical models, known as Toner–Tu or flocking theory, describe collections of 'dry', polar, self-propelled agents at any length scale, from flocks of flying birds to collections of polarized cytoskeletal filaments. In our case, *Toxoplasma gondii* actin filaments at the cell surface are propelled along by an underlying carpet of plus-end-directed myosin motors, whose action we can effectively capture as polarized filament self-propulsion. In Supplementary Information Sections 6 and 7, we provide a detailed explanation of the choice of our model, our equations and an intuitive interpretation for each term, a derivation of the curvature penalty term, the addition of filament polymerization and depolymerization into the model and our parameter choices. In Supplementary Information Section 8, we discuss the derivation of a tangential formulation of our filament self-organization equations using an extrinsic differential geometry approach, which is well-suited for numerical analysis using the finite element method. As discussed in detail in Supplementary Information Section 9, we used COMSOL Multiphysics[75] to solve our self-organization equations on triangular surface meshes of *Toxoplasma gondii* created from soft X-ray images of the extracellular *Toxoplasma gondii* tachyzoite cell shape using the SPHARM-PDM 3D Slicer package[76,77].

Statistics and reproducibility

Sample sizes: sample sizes were not determined a priori. For each experimental condition/replicate, we checked the robustness of our measurements by cell-to-cell and experiment-to-experiment comparisons and using statistical tests, when appropriate. Randomization: cells in experimental groups were random subsets of the same cell stock. In imaging experiments, individual wells or fields of view in imaging dishes were chosen at random for each experimental group. Blinding: analysis of motility modes across jasplakinolide concentrations (Supplementary Fig. 8) was performed blind to experimental condition and in a randomized order. Data exclusion: for speckle imaging experiments, we excluded cells with a fluorescent dye labelling density that was too low or too high to visualize and distinguish individual speckles. When tracking speckle movement, we analysed tracks that persisted for at least five frames (0.43 s). Assumptions of statistical tests: statistical tests performed on data in Supplementary Figs. 2 and 8 are discussed in detail in the text associated with those figures.

Reporting summary

Further information on research design is available in the Nature Portfolio Reporting Summary linked to this article.

Data availability

Toxoplasma gondii strains, plasmids and imaging data are available upon request. The BioNumbers database referenced in the Supplementary Information is available at https://bionumbers.hms.harvard.edu/search.aspx.

Code availability

MATLAB and COMSOL code is available at https://github.com/chueschen/Toxoplasma_actin.

References

61. Panas, M. W., Naor, A., Cygan, A. M. & Boothroyd, J. C. *Toxoplasma* controls host cyclin E expression through the use of a novel myr1-dependent effector protein, HCE1. *mBio* **10**, e00674–19 (2019).
62. Fox, B. A., Ristuccia, J. G., Gigley, J. P. & Bzik, D. J. Efficient gene replacements in *Toxoplasma gondii* strains deficient for nonhomologous end joining. *Eukaryot. Cell* **8**, 520–529 (2009).
63. Marino, N. D. et al. Identification of a novel protein complex essential for effector translocation across the parasitophorous vacuole membrane of *Toxoplasma gondii*. *PLoS Pathog.* **14**, e1006828 (2018).
64. Edelstein, A. D. et al. Advanced methods of microscope control using µManager software. *J. Biol. Methods* **1**, e10 (2014).
65. Morimatsu, M., Mekhdjian, A. H., Chang, A. C., Tan, S. J. & Dunn, A. R. Visualizing the interior architecture of focal adhesions with high-resolution traction maps. *Nano Lett.* **15**, 2220–2228 (2015).
66. Galassi, M. *GNU Scientific Library: Reference Manual* (Network Theory, 2009).
67. Shaw, M. K. & Tilney, L. G. Induction of an acrosomal process in *Toxoplasma gondii*: visualization of actin filaments in a protozoan parasite. *Proc. Natl Acad. Sci. USA* **96**, 9095–9099 (1999).
68. Jacot, D. et al. An apicomplexan actin-binding protein serves as a connector and lipid sensor to coordinate motility and invasion. *Cell Host Microbe* **20**, 731–743 (2016).
69. Huff, J. The Airyscan detector from ZEISS: confocal imaging with improved signal-to-noise ratio and super-resolution. *Nat. Methods* **12**, i–ii (2015).
70. Parkinson, D. Y., Knoechel, C., Yang, C., Larabell, C. A. & Le Gros, M. A. Automatic alignment and reconstruction of images for soft X-ray tomography. *J. Struct. Biol.* **177**, 259–266 (2012).
71. Chen, J. H. et al. A protocol for full-rotation soft X-ray tomography of single cells. *STAR Protoc.* **3**, 101176 (2022).
72. Jaqaman, K. et al. Robust single-particle tracking in live-cell time-lapse sequences. *Nat. Methods* **5**, 695–702 (2008).
73. Cordelières, F. P. Manual Tracking, a plug-in for ImageJ software. *ImageJ* https://imagej.net/ij/plugins/track/track.html (2005).
74. Schindelin, J. et al. Fiji: an open-source platform for biological-image analysis. *Nat. Methods* **9**, 676–682 (2012).
75. COMSOL Multiphysics v.5.5. (COMSOLAB, 2019); www.comsol.com
76. Fedorov, A. et al. 3D Slicer as an image computing platform for the Quantitative Imaging Network. *Magn. Reson. Imaging* **30**, 1323–1341 (2012).
77. Vicory, J. et al. SlicerSALT: Shape AnaLysis Toolbox. *Shape Med. Imaging* **11167**, 65–72 (2018).

Author contributions

C.L.H. contributed to conceptualization, methodology, investigation, interpretation, visualization, funding acquisition, project administration, software and formal analysis, wrote the original paper draft and reviewed and edited the paper. L.S.-Z. contributed to conceptualization, investigation and interpretation and reviewed and edited the paper. J.-H.C. contributed to investigation. M.A.L. contributed to methodology. C.A.L. contributed to methodology and funding acquisition. J.C.B. contributed to conceptualization, interpretation, funding acquisition and resources and reviewed and edited the paper. R.P. contributed to conceptualization, methodology, interpretation, resources and formal analysis and reviewed and edited the paper. A.R.D. contributed to conceptualization, methodology, interpretation, funding acquisition, formal analysis and resources and reviewed and edited the paper.

Competing interests

The authors declare no competing interests.

Additional information

Supplementary information The online version contains supplementary material available at https://doi.org/10.1038/s41567-024-02652-4.

Correspondence and requests for materials should be addressed to Christina L. Hueschen or Alexander R. Dunn.

Peer review information *Nature Physics* thanks Daria Bonazzi, Arnold Mathijssen and Isabelle Tardieux for their contribution to the peer review of this work.

Reprints and permissions information is available at www.nature.com/reprints.

nature portfolio

Corresponding author(s): Alexander R. Dunn, Christina L. Hueschen

Last updated by author(s): 07/12/2024

Reporting Summary

Nature Portfolio wishes to improve the reproducibility of the work that we publish. This form provides structure for consistency and transparency in reporting. For further information on Nature Portfolio policies, see our Editorial Policies and the Editorial Policy Checklist.

Statistics

For all statistical analyses, confirm that the following items are present in the figure legend, table legend, main text, or Methods section.

n/a	Confirmed	
☐	☒	The exact sample size (*n*) for each experimental group/condition, given as a discrete number and unit of measurement
☐	☒	A statement on whether measurements were taken from distinct samples or whether the same sample was measured repeatedly
☐	☒	The statistical test(s) used AND whether they are one- or two-sided *Only common tests should be described solely by name; describe more complex techniques in the Methods section.*
☒	☐	A description of all covariates tested
☐	☒	A description of any assumptions or corrections, such as tests of normality and adjustment for multiple comparisons
☐	☒	A full description of the statistical parameters including central tendency (e.g. means) or other basic estimates (e.g. regression coefficient) AND variation (e.g. standard deviation) or associated estimates of uncertainty (e.g. confidence intervals)
☐	☒	For null hypothesis testing, the test statistic (e.g. *F*, *t*, *r*) with confidence intervals, effect sizes, degrees of freedom and *P* value noted *Give P values as exact values whenever suitable.*
☒	☐	For Bayesian analysis, information on the choice of priors and Markov chain Monte Carlo settings
☒	☐	For hierarchical and complex designs, identification of the appropriate level for tests and full reporting of outcomes
☒	☐	Estimates of effect sizes (e.g. Cohen's *d*, Pearson's *r*), indicating how they were calculated

Our web collection on statistics for biologists contains articles on many of the points above.

Software and code

Policy information about availability of computer code

Data collection	Micromanager version 1.4 software, ChimeraX version 1.0 software, and Zen 2.3 (black edition) software.
Data analysis	FIJI/ImageJ (Version 2.0.0-rc-69/1.52p), the ImageJ Manual Tracking plugin, u-track software (Danuser lab, release 2.2.0), and home-written custom MatLab code (Mathworks, version 2020a) available at https://github.com/chueschen/Toxoplasma_actin were used during data analysis.

For manuscripts utilizing custom algorithms or software that are central to the research but not yet described in published literature, software must be made available to editors and reviewers. We strongly encourage code deposition in a community repository (e.g. GitHub). See the Nature Portfolio guidelines for submitting code & software for further information.

Data

Policy information about availability of data

All manuscripts must include a data availability statement. This statement should provide the following information, where applicable:
- Accession codes, unique identifiers, or web links for publicly available datasets
- A description of any restrictions on data availability
- For clinical datasets or third party data, please ensure that the statement adheres to our policy

Plasmids, Toxoplasma gondii strains, and microscopy movies are available upon request. The BioNumbers database referenced in the Supplemental Information is available at https://bionumbers.hms.harvard.edu/search.aspx.

Human research participants

Policy information about studies involving human research participants and Sex and Gender in Research.

Reporting on sex and gender	N/A
Population characteristics	N/A
Recruitment	N/A
Ethics oversight	N/A

Note that full information on the approval of the study protocol must also be provided in the manuscript.

Field-specific reporting

Please select the one below that is the best fit for your research. If you are not sure, read the appropriate sections before making your selection.

☒ Life sciences ☐ Behavioural & social sciences ☐ Ecological, evolutionary & environmental sciences

For a reference copy of the document with all sections, see nature.com/documents/nr-reporting-summary-flat.pdf

Life sciences study design

All studies must disclose on these points even when the disclosure is negative.

Sample size	Sample sizes were not determined a priori. For each experimental condition/replicate, we checked the robustness of our measurements by cell-to-cell and experiment-to-experiment comparisons and using statistical tests, when appropriate. More on all experiments: Single-molecule velocity measurements in Fig. S2 were used to report that a larger fraction of actin molecules were mobile compared to myosin molecules. With the sample sizes used, this difference was clearly visible even qualitatively, by eye (see CDF, Fig S2D). Speed measurements in Fig. 1 were used to simply report a mean speed and standard deviation, and the number of measurements are shown to allow reader interpretation. Recirculation of jasplakinolide-stabilized bundles (Fig. 3C, S4) were used to provide a description of bundle speed and its oscillatory nature, and the number of measurements are shown to allow reader interpretation. The characterization of the frequency of gliding modes (Fig. S1, S8) were used to show a significant increase in bidirectional gliding with increasing jasplakinolide concentration. p-values for an ANOVA test on this metric are shown with Fig. S8 in the SI, and the sample sizes used allow for highly significant pairwise differences between conditions.
Data exclusions	For speckle imaging experiments, we excluded cells with a fluorescent dye labeling density that was too low or too high to visualize and distinguish individual speckles. For analysis of speckle movement, we only analyzed tracks that persisted for at least 5 frames (0.43 seconds).
Replication	For measurements of the velocities of actin or myosin molecules or actin protrusions, measurements were replicated in 6-18 independent cells per condition. For measurements of the frequency of cell gliding behaviors, 45-156 gliding events were measured from 3 independent rounds of experiment. As discussed in detail in the methods section on jasplakinolide treatment, recirculation of actin bundles (Fig. 3c, S4) is very sensitive to time and concentration of jasplakinolide treatment. Beyond 30 min of treatment, protrusions are stationary, as previously reported, likely because bundles grow long enough to reach back from the conoid into the cell body, preventing movement. We find this an interesting biological result and discuss this interpretation in the manuscript.
Randomization	Cells in experimental groups were random subsets of the same cell stock. Cells were settled into imaging dishes or wells; individual wells or fields of view were chosen at random for each experimental group.
Blinding	One experimental measurement where this kind of group allocation could be relevant are the single-molecule speed comparisons in Fig. S2. In that case, molecule detection and tracking was done by an automated algorithm (u-track, Danuser lab), which was "blind" to which group it was analyzing. The other is the analysis of motility modes across jasplakinolide concentrations (Fig. S8). Here, movies for different jasplakinolide concentrations were blinded during analysis (information about concentration was not shown) and analyzed in a random order.

Reporting for specific materials, systems and methods

We require information from authors about some types of materials, experimental systems and methods used in many studies. Here, indicate whether each material, system or method listed is relevant to your study. If you are not sure if a list item applies to your research, read the appropriate section before selecting a response.

Materials & experimental systems

n/a	Involved in the study
☐	☒ Antibodies
☐	☒ Eukaryotic cell lines
☒	☐ Palaeontology and archaeology
☒	☐ Animals and other organisms
☒	☐ Clinical data
☒	☐ Dual use research of concern

Methods

n/a	Involved in the study
☒	☐ ChIP-seq
☒	☐ Flow cytometry
☒	☐ MRI-based neuroimaging

Antibodies

Antibodies used	Mouse anti-tubulin monoclonal antibody DM1alpha (Sigma T6199; diluted 1:500), anti-mouse IgG secondary antibody conjugated to Alexa Fluor 488 (Cell Signaling 4408S, diluted 1:500).
Validation	This tubulin antibody has been validated by the manufacturer for this application (immunostaining) and used extensively by the microtubule research community. In this work, it was used to label the beautiful subpellicular microtubules of Toxoplasma gondii, which have a very well-defined organization - which was clearly recognizable in our imaging.

Eukaryotic cell lines

Policy information about cell lines and Sex and Gender in Research

Cell line source(s)	Toxoplasma gondii tachyzoite strains (sex and gender not relevant) were made from the Toxoplasma gondii type I RH hxgprt ku80 strain, which was a gift of John Boothroyd and his group. Human Foreskin Fibroblasts were obtained from the neonatal clinic at Stanford University following routine circumcisions that are performed at the request of the parents for cultural, health, or other personal medical reasons (i.e., not in any way related to research). These foreskins, which would otherwise be discarded, were fully deidentified and therefore do not constitute human subjects research.
Authentication	Cell lines were not authenticated by external/official means.
Mycoplasma contamination	Cell lines (human foreskin fibroblasts) tested negative for mycoplasma contamination.
Commonly misidentified lines (See ICLAC register)	No commonly misidentified cell lines were used.